Supplementary Materials for

Programmable hyperbolic polaritons in van der Waals semiconductors

A. J. Sternbach*†, S. H. Chae†, S. Latini, A. A. Rikhter, Y. Shao, B. Li, D. Rhodes, B. Kim, P. J. Schuck, X. Xu, X.-Y. Zhu, R. D. Averitt, J. Hone, M. M. Fogler, A. Rubio, D. N. Basov

*Corresponding author. Email: as5049@columbia.edu
†These authors contributed equally to this work.

This PDF file includes:

Materials and Methods

Note S1. Apparatus and materials

Experimental set-up

For nano-optical imaging experiments, we used a scattering-type scanning near-field optical microscope (s-SNOM, Neaspec). The atomic force microscope (AFM), with a tip radius of around 30 nm, operates in tapping-mode with a frequency of about 70 kHz and an amplitude of approximately 70 nm. The time-resolved psuedoheterodyne technique (*37*) is used to extract the amplitude (S) and phase (φ) of the near-field signal in imaging experiments (Fig. 3, figs. S4 and S6C) while time-resolved nano-FTIR (9, *30, 31*) is used to extract spectra of the near-field amplitude and phase (Figs. 1D, 2, and figs. S1, S2, and S5). The additive background contribution was strongly attenuated by considering only information modulated at the second or third harmonic of the tapping frequency of the AFM tip. The pump and probe channels derived from a 20 W; 1030 nm Yb:kGW amplified laser source operating at 750 kHz (Pharos, Light Conversion). The intense laser pulse was converted to the non-degenerate pump and probe channels by employing three optical parametric amplifiers (OPAs) and difference frequency generation (DFG). The narrowband DFG, used in imaging experiments, was generated by combining the fundamental 1030 nm output and an infrared idler beam (1080-2400 nm) from a two-stage non-colinear/colinear OPA in a 1.5 mm GaSe crystal. The pulse duration of the narrowband DFG (approximately 500 fs) was determined from electro-optic sampling measurements. The broadband DFG, used in spectroscopy experiments, was generated by combining a 1600 nm infrared beam generated in a two-stage colinear OPA with the tunable idler from the non-colinear/colinear generation scheme in a 1 mm GaSe crystal. The pulses were delivered to the Neasepc microscope with a well-controlled time delay, Δt, between their arrival controlled by a mechanical delay stage. For all data displayed in the main text the center wavelength of the pump was fixed in the range of 800-820 nm. Our experimental methods are discussed in Refs.(*34, 37*).

Material growth

The high quality WSe_2 crystals studied in our work were synthesized by self-flux method, then mechanically exfoliated onto an SiO_2/Si substrate (*38*).

Note S2. Model of the dielectric tensor

Model for the optical properties of WSe2

We model the dielectric response of WSe_2 with the tensor:

$$||\varepsilon|| = \begin{bmatrix} \varepsilon^{ab} & 0 & 0 \\ 0 & \varepsilon^{ab} & 0 \\ 0 & 0 & \varepsilon^{c} \end{bmatrix} \quad (S1)$$

Where $\varepsilon^{ab} = \varepsilon^{a} = \varepsilon^{b}$ and ε^{c} are the in-plane and out-of-plane components of the dielectric tensor, respectively. To obtain the components of the dielectric tensor we solve the Mott-Wannier (MW) model, Eq. (2) of the main text. Our solution provides the

eigenenergies, E, and wavefunctions, ψ, of the bound states (see supplementary note S6). The dielectric response is then computed with the Lorentz model (*28*):

$$\varepsilon^i = \varepsilon^i_{stat} + \frac{n_x e^2}{\varepsilon_0 m^i} \sum_{k=1}^N \frac{f^i_k}{(E_k/\hbar)^2 - \omega^2 - i\omega\gamma_k} \qquad \text{(S2)}$$

Where the subscript i is used to indicate the crystallographic axis (i=a, b, or c). The summation variable k represents the orbital and quantum number of the transition. The photon energy is given by ω while ε_0 and e are fundamental constants representing the permittivity of free space and electron charge respectively. Additionally, the Lorentz model parameters, $n_x, \varepsilon^i_{stat}, m^i$, describe the carrier density, static permittivity and effective mass of WSe$_2$. The remaining parameters γ_k, and E_k describe the linewidth and resonant energy of a given transition. We take $\gamma_k = \gamma$ to be the same for all transitions. The oscillator strength is proportionate to f^i_k, calculated as:

$$f^i_k = \frac{2m^i}{\hbar^2} |E_{1s} - E_k| |\langle \psi_{1s} | \vec{r} \cdot \hat{e}_i | \psi_k \rangle|^2 \qquad \text{(S3)}$$

Where the matrix elements, $d_i = \langle \psi_{1s} | \vec{r} \cdot \hat{e}_i | \psi_k \rangle$, are computed along the relevant axis of the dielectric tensor (with i= x, y and z representing the a, b and c axes, respectively). The energy difference, $\Delta E = |E_{1s} - E_k|$, is relative to the 1s state. These parameters are given in table S2. The undetermined variables, the bound-carrier density, n_x, and linewidth, γ are extracted by comparing the observables in our experiment with the predictions of the anisotropic MW model.

The fluence dependent increase of n_x (Fig. 2C of the main text) is fit with the standard formula for saturable absorption:

$$n_x = \frac{\alpha P}{(1 + P/P_0)} \quad \text{(S4)}$$

The parameters $\alpha = 7 \times 10^{18}$ cm^{-3} mW^{-1} and $P_0 = 6$ mW are extracted from the fits.

Supplementary Text

Note S3. WSe$_2$ in the steady state

To determine the dielectric response of WSe$_2$ in the steady-state we performed nano-Fourier transform infrared (FTIR) spectroscopic measurements. The raw data are impacted by a frequency-dependent instrumental response, which includes frequency dependence of the intensity, the detector responsivity and other extrinsic factors. The data presented in Fig. S1 are normalized to gold, which is a common procedure used to eliminate the instrumental response (*32*). In Fig. S1 we display the third harmonic of the near-field amplitude and phase recorded in the steady-state on a WSe$_2$ flake with approximately 100 nm thickness, exfoliated onto an SiO$_2$ (285 nm)/Si substrate. Deviations from a featureless response, which are observed in the frequency range of 1000-1150 cm^{-1}, are attributed to

the SiO_2 phonon. As described in Ref. (*39*) in the special case that the components of the dielectric tensor are featureless, they can be extracted by quantitatively analyzing the degree to which a phonon in an underlying substrate is screened. From the latter inversion procedure, we obtain the principle values of the dielectric tensor, $\varepsilon_1^{ab} = 13.7_{-2.0}^{+6.0}$, $\varepsilon_2^{ab} = 0.0_{-0.0}^{+0.0}$, $\varepsilon_1^c = 4.0_{-0.9}^{+4.5}$, and $\varepsilon_2^c = 0.0_{-0.0}^{+0.0}$, which are independent of the probe frequency in the range 700-1150 cm^{-1} in the steady state.

Note S4. Transient electrodynamics of WSe₂

In our previous work, we observed about 10% bleaching of the A-exciton driven by red-detuned photoexcitation (*34*). Here, we employ a pump laser with 750 kHz repetition rate and with lower photon energy (central energy in the range of 1.51-1.55 eV). We estimate the strongest photo-excitation conditions employed in this work corresponds to approximately 2-3× lower absorbed fluence than employed in Ref. (*34*). Taking the dependence of the bleaching on the excitation density to be within a linear regime we, therefore, estimate 5% as the upper limit for the photo-induced decrease of the A-exciton oscillator strength. Our estimate does not account for photo-induced heating, and other sources of spectral broadening, and is likely an overestimate. Thus, while our excitation density may be approaching the onset of the Mott-transition, we conclude that excitons dominate the population of optically generated electron-hole pairs.

After photo-exciting the WSe₂ crystal, drastic changes of the frequency dependent near-field amplitude and phase are observed (Fig. 2 of the main text). We utilized a photon energy of about 12,180 cm^{-1} (= 1.51 eV), which is red-detuned from the optical gap of WSe₂ where absorption is dominated by the A-exciton resonance. Red detuning was essential to realize a sufficiently large penetration depth of the pump radiation (approximately 600 nm) to uniformly photo-excite the 300-500 nm thick WSe₂ crystals studied in the main text. To supplement the data presented in Fig. 2 of the main text we additionally show the pump-induced changes of the near-field phase (fig. S2B) for the same dataset. In addition, all data used to extract the parameters reported in Fig. 2B and 2C of the main text and fig. S2E of the supplementary materials are shown in fig. S2C and S2D. Our experimental transient spectra were fit to extract quantitative information. We computed the dielectric response with the MW model as described in notes S2 and S6 for a set of trial parameters n_x and γ. The amplitude and phase spectra were then computed with the lightning rod-model (*32*). These parameters were adjusted until satisfactory agreement between the model and the experimental data, shown in figs. S2A, S2B, S2C and S2D, were obtained. The extracted spectral linewidth of the QT resonances, γ, (supplementary note S2) is displayed in fig. S2E. Linewidths in the range of 20-50 meV are typically extracted from our fits.

We stress that the model utilized to fit the FTIR data (Fig. 2 and fig. S2) is essentially a simple Lorentz oscillator model, see Eq. (S2). The parameters of the model, i.e. oscillator strength and spectral linewidth, are obtained from fitting our data. While the final parameter of the model, the resonant frequency of the oscillators, is obtained from a solution to the MW model (see note S6) these frequencies all lie below the low energy cutoff of our detector. Therefore, the infrared electrodynamics calculated by our model

display weak sensitivity to the exact resonant energies, provided that they remain below our detectable spectral range. Further, the Tr-FTIR data of Fig. 2 of the main text and fig. S2 can be adequately fit with any choice of the anisotropy parameter, κ. Thus, the only requirements for the simple Lorentz oscillator model (Eq. S2) to reveal good agreement with our FTIR data (Fig. 2 and fig. S2) are zero crossing of the in-plane component of the real part of the dielectric function at the frequency $\omega_{0,ab}$ and an appropriate spectral linewidth, γ, of the oscillator.

A characteristic edge is observed in the normalized transient near-field amplitude spectra, S_p/S_r, which crosses the one-hundred percent line at approximately the same frequency where a peak is observed in the normalized near-field phase spectra, ϕ_p-ϕ_r. The subscripts, p and r, are used to indicate whether data were recorded under photo-excited or steady state conditions respectively. The zero-crossing frequency $\omega_{0,ab}$ (fig. S3A) is identified approximately where S_p/S_r crosses the one-hundred percent line, and ϕ_p-ϕ_r shows a peak (arrows in figs. S2A and S2B).

Principle values of the dielectric tensor extracted from fitting our experimental data (figs. S2A and S2B) are shown in fig. S3A. The dielectric tensor obtained from the MW model, with an experimentally realistic electron-hole pair density, was then used to calculate the imaginary component of the momentum-dependent reflectance co-efficient, $\text{Im}\{R_p\}$, which governs the dispersion relationship in WSe$_2$. The trend of $\text{Im}\{R_p\}$ is plotted against momentum and probe frequency in fig. S3A. Maxima of $\text{Im}\{R_p\}$ dictate the energy-momentum dispersion relationship of propagating waveguide modes. The dispersion of confined hyperbolic polaritons is evident in the dispersion relation of fig. S3 in agreement with our experimental data (Figs. 1-3 of the main text).

We proceed to discuss inhomogeneous intensity variations observed in our data, fig. S4. A series of disks patterned on an SiO$_2$ substrate are shown in fig. S4A. A 440 nm thick WSe$_2$ flake was transferred on top of these antennas. In the steady state, inhomogeneous variations in the scattering amplitude are observed. The inhomogeneous intensity patterns are reminiscent of antenna modes, which are directly observed in images of the near-field amplitude collected on exposed gold disks (40). The magnitude of these inhomogeneous intensity variations decreases as the disk diameter decreases, which is consistent with the expectations of antenna modes. Further, as the WSe$_2$ crystal is an anisotropic dielectric in the steady state (see note S3) these intensity variations are unrelated to conical hyperbolic ray propagation. The imaging data shown in Figs. 3B and 3C were Fourier filtered to reduce the background intensity variations associated with the polarized antenna launchers. The antenna modes are highly directional (fig. S4) and could be avoided, without Fourier filtering, in line profiles selected for quantitative analysis in Fig. 3F of the main text by considering data over a limited angular range (see Fig. 3B of the main text).

Next, we address dispersion of the hyperbolic waveguide modes in optically excited WSe$_2$ and compare the results to the predictions of the same MW theoretical model that we employed to understand the pump-probe spectra in Fig. 2A. We focus our analysis on the inner ring because geometric factors lead to an improved signal-to-noise ratio for the

inner hyperbolic rays, see Fig. 3F of the main text. The experimental results (fig. S5B) are in accord with the theoretically calculated dispersion (fig. S5C). In particular, the coordinates where the maxima of S are observed evolves with ω in a fashion agreeing with the theoretical calculations (Fig. 1D of the main text).

Note S5. Hyperbolic electrodynamic simulations

The model consists of a thin slab of WSe$_2$ placed on SiO$_2$/Si substrate as depicted in fig. S6A. An antenna in the form of a gold strip of negligible thickness is located at the interface of the WSe$_2$ and SiO$_2$ layers. Although in the experiment the antenna has the shape of a disk instead of the strip, this simplified one-dimensional model retains the main physically relevant feature, namely, a sharp edge of the conductor. Such an edge can act as a polariton launcher when an external electric field E_0 has a component normal to the edge, in this case, along the x-direction (see fig. S6A). Similar to Ref. (*41*), we assume that the tip of the near-field microscope serves mainly as a detector of the local field in the z-direction (parallel to the tip), and so the tip is not explicitly included in the simulation. However, the analytical solution of the problem presented in Ref. (*41*) does not apply to the present case because of the in-plane inhomogeneity, see fig. S6B and text below.

Due to the smallness of the strip compared to the probe wavelength, the quasi-static approximation is appropriate, where the electric field is expressed as a gradient of a scalar potential $\Phi(\mathbf{r})$. This potential obeys the generalized Laplace equation containing the permittivity tensor $\varepsilon^{\mu\nu}(\mathbf{r})$:

$$\nabla_\mu \varepsilon^{\mu\nu}(\mathbf{r})\nabla_\nu \Phi(\mathbf{r}) = 0 \ (S5)$$

We impose the boundary condition $\Phi = -E_0 x$ at the boundary of the simulation cell to represent the condition that the field becomes equal to E_0 at large distances. The gold strip is taken to be perfectly conducting, implying $\Phi(\mathbf{r}) = $ const on the strip. The permittivity $\varepsilon^{\mu\nu}(\mathbf{r})$ is taken to be isotropic and uniform for SiO$_2$ and Si. The permittivity of WSe$_2$ is a diagonal tensor with in-plane and out-of-plane principal values ε^{ab} and ε^c, respectively. The dielectric tensor is modified by the pump and can have a considerable spatial variation caused by a mirror-like reflection of the pump beam by the antenna. We model the latter inhomogeneity using two adjustable parameters listed in Table S1: the ratio $C = n_{in}/n_{out}$ of the photo-excited carrier densities far and near the antenna and the characteristic width d_{diff} of the crossover region. The carrier density profile is depicted in fig. S4B. The physical origin of d_{diff} is the finite width of the pump-beam. The density ratio n_{in}/n_{out} originates from the difference in the intensity of pump radiation in the far and near regions. Due to the large in-plane dielectric constant of WSe$_2$ at the pump wavelength, the reflected pump beam propagates nearly parallel to the z-axis. Therefore, within the simplest geometrical optics approximation, the total light intensity of the pump over the antenna is twice larger than away from it. Since the carrier density is expected to exhibit a saturable absorption effect (see Fig. 2C of the main text) the ratio of n_{in}/n_{out} should be smaller than the factor of two and decrease with increasing fluence, which is in agreement with the extracted values of C.

In our fitting procedure, for each trial set of parameters, we solved Eq. (S5) numerically for the z-component of the electric field above the top surface of WSe2. We then demodulated this quantity at the second harmonic of the tip tapping frequency to obtain the near-field signal $E_{nf}(x)$. The results are presented in Fig. 3 of the main text. The two peaks in the signal located roughly symmetrically on each side of the antenna's edge are due to the polaritonic rays, as described in the main text. The polaritonic rays are observed on the top surface of WSe2 at a lateral distance, δr, relative to the edge of the gold antennae. As the gold antennae are underneath the surface of the crystal and are not directly observed in our experiment the absolute positions of δr in data shown in Figs. 1D, 3F, and fig. S5B are determined by matching a line-profile of experimental data at a single fluence (Fig. 3F) or single probe frequency (Fig. 1D and fig. S5B) with the theoretical line profile. The absolute positions are then constrained for the remaining sets of co-located experimental data. The absolute positions are in accord with the known disk radius (Fig. 3A) relative to the diameters of the concentric 'hot rings' observed in the scattering amplitude (see Figs. 3C and 3D of the main text). The characteristic peak in the scattering amplitude observed close to the disk edge is due to the step-like change of the permittivity of WSe2 in our model. The sharpness and height of this latter peak depends on the fitting parameters, C and d_{diff}. We stress that the simulation results reproduce the two characteristic peaks at $\delta r = d|\tan(\theta)|$, where d is the crystal thickness and θ is the angle from the surface normal as in Ref. *(41)*, if the system is homogeneous (i.e. C = 1). Further, in the latter, homogeneous, case the central peak is not observed. A reasonable match between the experimental data and simulations is achieved for the set of parameters given in table S1.

Lastly, to construct the two-dimensional image depicted in Fig. 3D of the main text, we did the following: First, we multiplied our one-dimensional near-field profiles E_{nf} (with x set to r) by the cosine of the in-plane polar angle ϕ to achieve an approximate mapping between the solutions for the strip and for the disk. This $\cos\phi$ factor takes into account that the polarization of the antenna is mainly due to the component of the external field normal to the edge, as mentioned earlier. Additionally, to match the experimentally observed images, we found it necessary to supplement the result with another, radially symmetric term:

$$E_z(r, \phi) = E_{ff}(r) + E_{nf}(r) \cos\phi \qquad \text{(S6)}$$

The added term $E_{ff}(r)$ presumably comes from the far-field background, which is not included in our simulations.

Note S6. The Mott-Wannier model

The Mott-Wannier (MW) model provides an accurate and efficient description of the excitonic properties for a large variety of semiconductors. Specifically, for TMDs it has been extensively reported to agree very well with experiments and the first-principles counterpart, i.e. the Bethe-Salpeter method, Refs. *(29, 42, 43)*. In short, the MW method models the relative motion between the electron and the hole forming the exciton with a simple hydrogen-like Hamiltonian where the Coulomb interaction accounts for the

screening provided by all the other electrons in the material. The main assumption behind the MW model is that the exciton has to be localized in a portion of the Brillouin zone where both the energy dispersion of the electron and the hole can be well described by a paraboloid, which is the case for WSe$_2$.

Given the layered nature of bulk TMDs, the MW model needs to be adapted in order to describe the intrinsic anisotropy arising from the different values of the excitonic effective masses and the dielectric screening in the in-plane and out-of-plane directions. This can be easily done by separating the in-plane motion from the out-of-plane one as done in Ref. (29). The resulting Hamiltonian can then be written as:

$$\left\{ -\frac{\hbar^2}{2m^{ab}}\left(\frac{d^2}{dx_{eh}^2} + \frac{d^2}{dy_{eh}^2}\right) - \frac{\hbar^2}{2m^c}\frac{d^2}{dz_{eh}^2} - V(\vec{r}_{eh}) \right\}\psi = E_{eh}\psi, \qquad (S7)$$

where the potential is given by:

$$V(\vec{r}_{eh}) = \frac{e^2}{4\pi\varepsilon_0\sqrt{\varepsilon_{stat}^{ab}\varepsilon_{stat}^c}(x_{eh}^2+y_{eh}^2+(\varepsilon_{stat}^{ab}/\varepsilon_{stat}^c)z_{eh}^2)^{1/2}}. \qquad (S8)$$

After conveniently rescaling the above equations with $a_x^* = \left(\frac{m_0}{m^{ab}}\right)\sqrt{\varepsilon_{stat}^{ab}\varepsilon_{stat}^c}a_0$, $a_z^* = \left(\frac{m_0}{\sqrt{m^{ab}m^c}}\right)\sqrt{\varepsilon_{stat}^{ab}\varepsilon_{stat}^c}\,a_0$, $Ha^* = \frac{m^{ab}}{(m_0\varepsilon_{stat}^{ab}\varepsilon_{stat}^c)}Ha$ and $E_{eh} = Ha^*E$ with a_0 being the hydrogen Bohr radius and m_0 the electron mass, we obtain Eq. (2) of the main text (note that there the electron-hole relative distance r is also rescaled, i.e. $\vec{r} = (a_x x, a_y y, a_z z)$). The solution to the MW problem described above allows us to determine the energies of the Rydberg series and the respective wavefunctions.

The parameters used in the Hamiltonian have been calculated ab-initio. For red-detuned photo-excitation, with photo-induced electron-hole pair densities below the Mott threshold, the electron-hole pairs form direct excitons (zero momentum excitons) localized at the K-valley. Thus, we consider momentum direct electron-hole pairs. The effective masses are extracted from density functional theory (DFT) electronic band structures calculated around the K-valley. The in-plane and out-of-plane static dielectric constants are calculated using linear response theory at the random-phase approximation (RPA) level starting from local-density approximation (LDA) wavefunctions. As for the numerical details, the MW problem has been solved with the Octopus code (44) on a real space grid, making sure that convergence on both box size and grid spacing was reached on the Rydberg states energy. We calculated specific values with the interlayer spacing of $d_{int} = 0.67\ nm$ yielding the parameters used in the main text: $m^{ab} = 0.2$, $m^c = 1.6$, $\varepsilon_{stat}^{ab} = 13.4$ and $\varepsilon_{stat}^c = 8.3$. Thus, the anisotropy parameter $\kappa = (\varepsilon_{stat}^{ab}m^{ab})/(\varepsilon_{stat}^c m^c) = 0.8$ is obtained. The precise values of the static permittivity and masses depend on the interlayer spacing. Experimentally, fits with acceptable quality can be achieved for a wide range of values of κ. Pump-probe nano-THz experiments are best suited to establish a precise experimental bound of κ, which would require experimental technology that has not yet been demonstrated.

The solution of the MW eigensystem allows us to readily calculate the transition energies and matrix elements of the light-driven internal quantum transitions among the Rydberg states. These matrix elements are nothing else than the expectation value of the dipole operator between different Rydberg states. In table S2 we report the dipole expectation values for WSe_2 in all directions between the lowest excitonic state, the 1s, to all the others Rydberg states, i.e. the matrix elements appearing in Eqs. (S2) and (S3) of note S2. As a reference the energy of the 1s state is $E_{1s} = -38.2 \, meV$. We remark that below the 1s-2p resonant energy the Mott-Wannier model predicts an increase of the principal values of the dielectric tensor. Thus, our model accounts for broadband hyperbolicity which supported in a broad range of infrared frequencies above about 30 meV and predicts that hyperbolicity should vanish at the lowest THz frequencies.
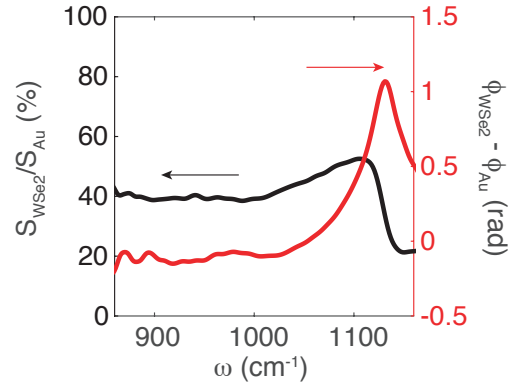
Fig. S1. Steady-state spectroscopy.

The third harmonic of the scattering near-field amplitude (black; left vertical axis) and phase (red; right vertical axis) were obtained by nano-FTIR spectroscopy on WSe$_2$ and normalized to the spectra recorded on gold (Au).
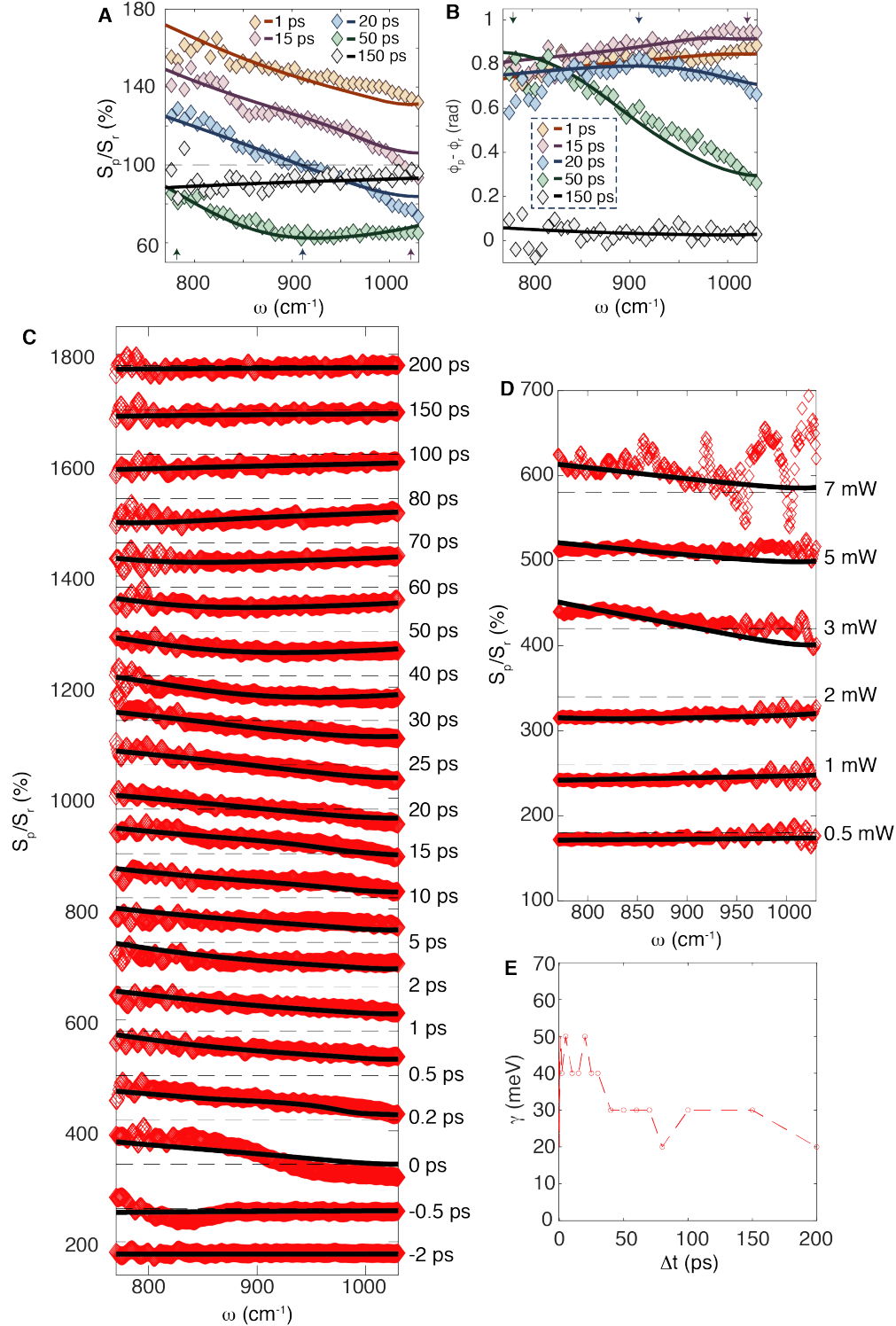
Fig. S2. Dynamics of the Nano-FTIR Spectroscopy.

A representative series of normalized near-field (**A**) amplitude, S_p/S_r, and (**B**) phase $\phi_p-\phi_r$, spectra are shown. The photo-excited spectra (diamonds) are color coded according to pump probe time delay given in the legend in units of ps when the photo-excited near-field

amplitude and phase, S_p and ϕ_p, data were recorded. The reference amplitude and phase, S_r and ϕ_r, data were recorded at the time delay of $\Delta t = -8$ ps. The phase spectra are vertically offset. The solid lines were calculated with the lightning rod formalism using the MW model (see note S6) with the carrier density n_x (Fig. 2B of the main text) and scattering rate, γ (panel D) and are also color coded according to the time-delay (legend). (**C**) The full set of near-field amplitude data for the time-dependance sequence (red diamonds) and the corresponding model fits (black lines) computed with the parameters reported in Fig. 2B of the main text and in panel E. The curves are vertically offset, and the time delay when the S_p spectra were collected are indicated to the right of the figure. (**D**) The near-field amplitude data recorded at a series of pump powers, indicated to the right of the figure (red diamonds). The corresponding model fits (black lines) computed with the parameters reported in Fig. 2C of the main text are overlaid. The same vertical offset applied to the data is applied to the 100% lines (black dashed lines) which are shown for each data set for reference in panels C and D. (**E**) The scattering rate extracted from the time-resolved nano-spectroscopy data in panels A, B, and C.
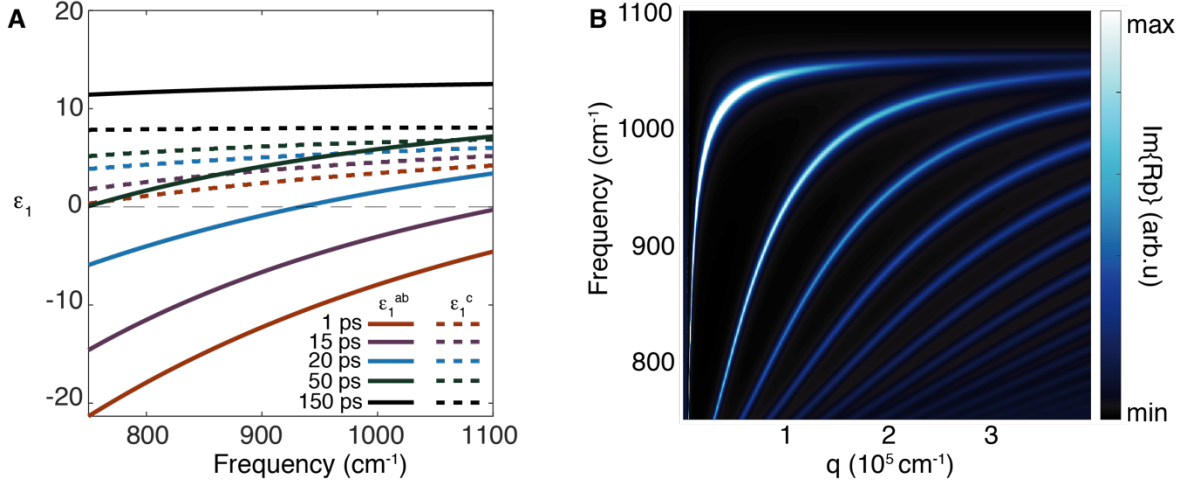
Fig. S3. Transient dispersion relationship in WSe₂.

(**A**) Principal values of the dielectric tensor in the transient state. (**B**) The imaginary component of the finite momentum reflection coefficient $\mathrm{Im}\{R_p\}$ is plotted against momentum, q, and frequency, ω. The calculated results are for a 350 nm WSe₂ slab. A reduced scattering rate of $\gamma = 1$ meV was used for clarity with a carrier density of $n_x = 1.8 \times 10^{18}$ cm^{-3}.
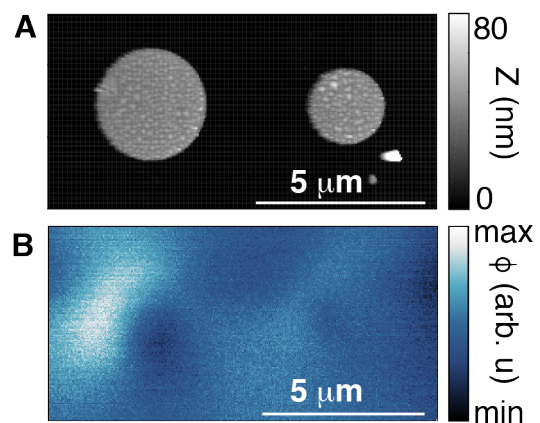
Fig. S4. Background Intensity.

A) Topography of exposed antennas. **B)** Near-field phase, ϕ, measured with a probe wavelength of 910 cm^{-1} before photoexcitation. The scale bars in panels A and B are 5 μm in length.
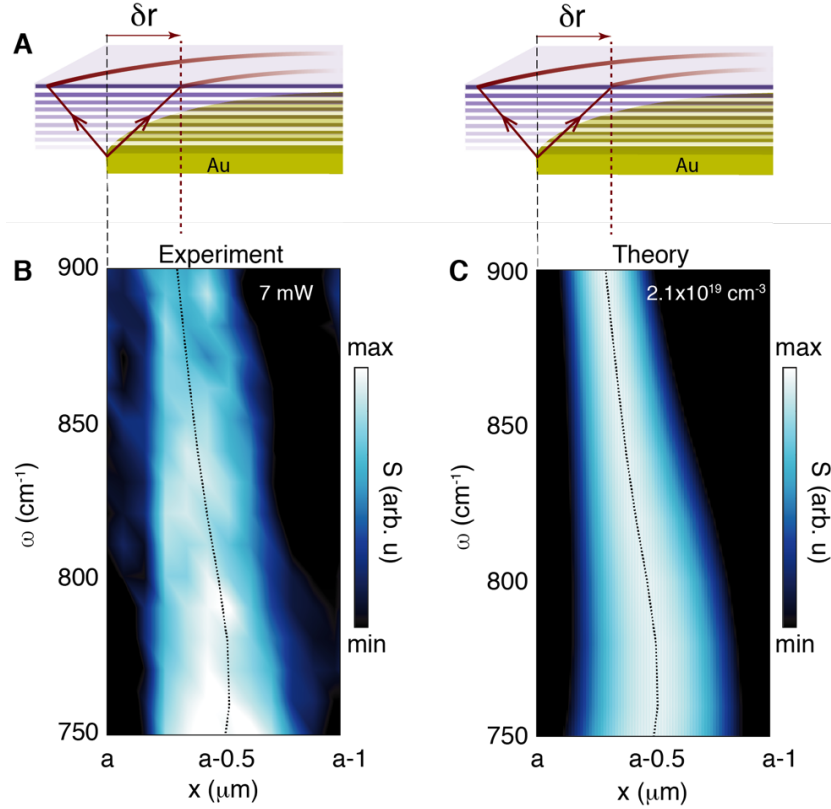
Fig. S5. Frequency dependence of hyperbolic polaritons revealed by hyperspectral nano-imaging.
(**A**) Schematics of the experiment. A gold disk underneath a WSe$_2$ crystal, with thickness d, launches hyperbolic rays which travel to the top surface of the crystal. (**B**) Experimental data recorded with a 7 mW pump at $\Delta t = 2$ ps on a 380 nm thick flake of WSe$_2$ are displayed as a function of the probe frequency ω, revealing dispersion of the hyperbolic ray. (**C**) The calculated dispersion of the hyperbolic ray using the same parameters as the 7 mW data of Fig. 3F of the main text (see table S1) as input to the MW model (supplementary notes S5 and S6). The locations where maxima of the scattering amplitude are observed, δr, observed in the theoretical calculations are overlaid in panels (B) and (C) (dashed lines).
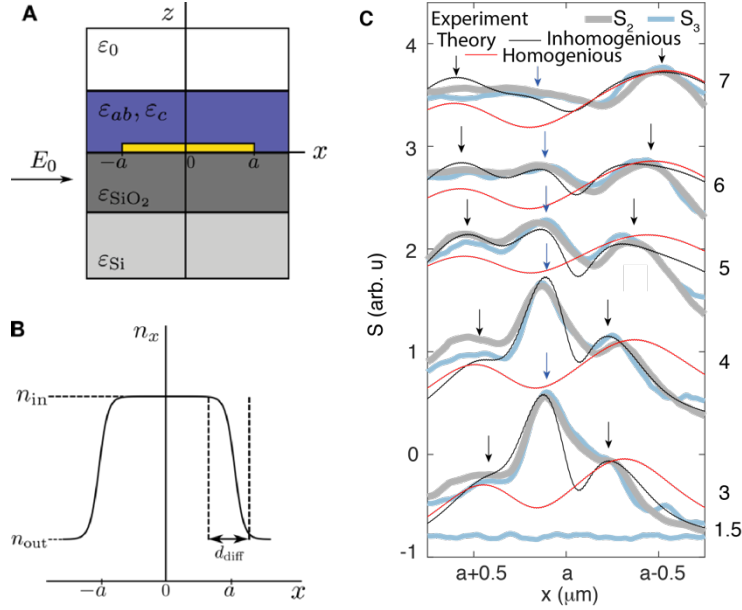
Fig. S6. Schematic depiction of the theoretical model.
(**A**) Geometry of our model. The substrate is a 285 nm layer of SiO_2 on top of Si with the permittivities ε_{SiO2} and ε_{Si} respectively. The sample has anisotropic permittivity described by a dielectric tensor (see note S2) with in and out of plane components ε_{ab} and ε_c respectively. The slab sits on top of a gold antenna with radius a. The superstrate is air with the permittivity of free space ε_0. The electric field is given by E_0. (**B**) Carrier density profile as a function of the real space coordinate x. (**C**) Predictions of the model are compared with experimental data. The model results with the inhomogeneous parameters reported in Table S1 are shown with black curves while the results with a homogeneous carrier density profile (where C = 1) produce the red curves. The second (gray) and third (light blue) harmonics of the experimental near-field amplitude data are also shown.

P (mW)	C, n_{in} / n_{out}	d_{diff}(nm)	n_{in} (× 10¹⁹ cm⁻³)	γ (meV)
3	1.35	170	1.6	32
4	1.3	170	1.7	33
5	1.15	170	1.9	35
6	1.1	170	2.0	35
7	1.07	230	2.1	33

Table S1. Parameters of the model.
Fitting parameters used for traces displayed in Fig. 3F of the main text. The theoretical calculations displayed in Figs. 1D and fig. S5B were produced with the parameters given for P = 7 mW.

ΔE (meV)	d_x (Å)	d_y (Å)	d_z (Å)
24.20	3.75E-07	1.97E-08	1.48E+01
27.40	3.36E-05	1.21E-05	8.37E-07
30.46	5.42E+00	2.60E+01	5.60E-05
30.46	2.60E+01	5.42E+00	9.87E-05
31.69	4.26E-04	1.60E-03	5.17E+00
32.71	3.01E-04	1.06E-03	7.61E-05
33.67	2.75E-03	1.14E-03	6.31E-04
33.67	4.31E-03	3.06E-03	6.69E-04
34.03	5.55E-02	1.10E-02	2.55E-04
35.13	6.36E+00	1.32E+01	3.15E-03
35.13	1.32E+01	6.37E+00	4.54E-03
35.37	7.47E-02	1.07E-01	2.66E-03
35.37	1.81E-01	4.68E-02	4.22E-03
36.07	9.44E-03	3.82E-02	2.05E+00
36.55	3.46E+00	4.59E+00	3.87E-03
36.58	4.51E+00	3.22E+00	1.59E-01
36.86	3.46E-01	5.89E-02	3.85E+00
37.15	4.64E-02	2.22E-01	2.97E-02
37.17	3.11E-02	2.31E-01	7.34E-02
37.20	4.44E-01	4.43E-01	9.81E-02
37.71	3.82E-01	1.77E-01	2.64E-02
37.75	3.07E-01	1.22E-01	1.06E-02
38.10	1.03E+00	9.31E-02	8.62E-02
38.11	2.48E-01	8.28E-04	5.69E-02
38.86	6.32E-01	1.79E-01	1.96E-02
39.07	2.96E-01	1.01E+00	6.06E-03
39.19	9.22E-01	1.90E-02	1.02E-01
39.67	3.46E+00	8.78E-01	1.30E-01
40.16	5.43E+00	6.26E+00	3.59E-01

Table S2. **Transition energies and dipole matrix elements.**
The transition energies and matrix elements between the lowest excitonic state (1s) and the rest of the Rydberg series states are given. Note that the states are ordered from low to high energy.

References and Notes

1. K. S. Novoselov, A. Mishchenko, A. Carvalho, A. H. Castro Neto, 2D materials and van der Waals heterostructures. *Science* **353**, aac9439 (2016). doi:10.1126/science.aac9439 Medline

2. G. Wang, A. Chernikov, M. M. Glazov, T. F. Heinz, X. Marie, T. Amand, B. Urbaszek, *Colloquium* : Excitons in atomically thin transition metal dichalcogenides. *Rev. Mod. Phys.* **90**, 021001 (2018). doi:10.1103/RevModPhys.90.021001

3. R. K. Fisher, R. W. Gould, Resonance cone structure in warm anisotropic plasma. *Phys. Lett. A* **31**, 235–236 (1970). [doi:10.1016/0375-9601(70)90946-1](doi:10.1016/0375-9601(70)90946-1)

4. J. Taboada-Gutiérrez, G. Álvarez-Pérez, J. Duan, W. Ma, K. Crowley, I. Prieto, A. Bylinkin, M. Autore, H. Volkova, K. Kimura, T. Kimura, M.-H. Berger, S. Li, Q. Bao, X. P. A. Gao, I. Errea, A. Y. Nikitin, R. Hillenbrand, J. Martín-Sánchez, P. Alonso-González, Broad spectral tuning of ultra-low-loss polaritons in a van der Waals crystal by intercalation. *Nat. Mater.* **19**, 964–968 (2020). [doi:10.1038/s41563-020-0665-0](doi:10.1038/s41563-020-0665-0) Medline

5. K. Chaudhary, M. Tamagnone, M. Rezaee, D. K. Bediako, A. Ambrosio, P. Kim, F. Capasso, Engineering phonon polaritons in van der Waals heterostructures to enhance in-plane optical anisotropy. *Sci. Adv.* **5**, eaau7171 (2019). doi:10.1126/sciadv.aau7171 Medline

6. T. Low, A. Chaves, J. D. Caldwell, A. Kumar, N. X. Fang, P. Avouris, T. F. Heinz, F. Guinea, L. Martin-Moreno, F. Koppens, Polaritons in layered two-dimensional materials. *Nat. Mater.* **16**, 182–194 (2017). doi:10.1038/nmat4792 Medline

7. K.-D. Park, M. A. May, H. Leng, J. Wang, J. A. Kropp, T. Gougousi, M. Pelton, M. B. Raschke, Tip-enhanced strong coupling spectroscopy, imaging, and control of a single quantum emitter. *Sci. Adv.* **5**, eaav5931 (2019). doi:10.1126/sciadv.aav5931 Medline

8. S. Dai, Z. Fei, Q. Ma, A. S. Rodin, M. Wagner, A. S. McLeod, M. K. Liu, W. Gannett, W. Regan, K. Watanabe, T. Taniguchi, M. Thiemens, G. Dominguez, A. H. Castro Neto, A. Zettl, F. Keilmann, P. Jarillo-Herrero, M. M. Fogler, D. N. Basov, Tunable phonon polaritons in atomically thin van der Waals crystals of boron nitride. *Science* **343**, 1125–1129 (2014). doi:10.1126/science.1246833 Medline

9. M. A. Huber, F. Mooshammer, M. Plankl, L. Viti, F. Sandner, L. Z. Kastner, T. Frank, J. Fabian, M. S. Vitiello, T. L. Cocker, R. Huber, Femtosecond photo-switching of interface polaritons in black phosphorus heterostructures. *Nat. Nanotechnol.* **12**, 207–211 (2017). doi:10.1038/nnano.2016.261 Medline

10. W. Ma, P. Alonso-González, S. Li, A. Y. Nikitin, J. Yuan, J. Martín-Sánchez, J. Taboada-Gutiérrez, I. Amenabar, P. Li, S. Vélez, C. Tollan, Z. Dai, Y. Zhang, S. Sriram, K. Kalantar-Zadeh, S.-T. Lee, R. Hillenbrand, Q. Bao, In-plane anisotropic and ultra-low-loss polaritons in a natural van der Waals crystal. *Nature* **562**, 557–562 (2018). [doi:10.1038/s41586-018-0618-9](doi:10.1038/s41586-018-0618-9) Medline

11. M. Mrejen, L. Yadgarov, A. Levanon, H. Suchowski, Transient exciton-polariton dynamics in WSe_2 by ultrafast near-field imaging. *Sci. Adv.* **5**, eaat9618 (2019). doi:10.1126/sciadv.aat9618 Medline

12. F. Hu, Y. Luan, M. E. Scott, J. Yan, D. G. Mandrus, X. Xu, Z. Fei, Imaging exciton–polariton transport in MoSe2 waveguides. *Nat. Photonics* **11**, 356–360 (2017). doi:10.1038/nphoton.2017.65

13. P. Li, I. Dolado, F. J. Alfaro-Mozaz, F. Casanova, L. E. Hueso, S. Liu, J. H. Edgar, A. Y. Nikitin, S. Vélez, R. Hillenbrand, Infrared hyperbolic metasurface based on nanostructured van der Waals materials. *Science* **359**, 892–896 (2018). doi:10.1126/science.aaq1704 Medline

14. M. Chen, X. Lin, T. H. Dinh, Z. Zheng, J. Shen, Q. Ma, H. Chen, P. Jarillo-Herrero, S. Dai, Author correction: Configurable phonon polaritons in twisted α-MoO₃. *Nat. Mater.* **19**, 1372 (2020). doi:10.1038/s41563-020-0781-x Medline

15. G. Hu, Q. Ou, G. Si, Y. Wu, J. Wu, Z. Dai, A. Krasnok, Y. Mazor, Q. Zhang, Q. Bao, C.-W. Qiu, A. Alù, Topological polaritons and photonic magic angles in twisted α-MoO₃ bilayers. *Nature* **582**, 209–213 (2020). doi:10.1038/s41586-020-2359-9 Medline

16. J. Duan, N. Capote-Robayna, J. Taboada-Gutiérrez, G. Álvarez-Pérez, I. Prieto, J. Martín-Sánchez, A. Y. Nikitin, P. Alonso-González, Twisted nano-optics: Manipulating light at the nanoscale with twisted phonon polaritonic slabs. *Nano Lett.* **20**, 5323–5329 (2020). doi:10.1021/acs.nanolett.0c01673 Medline

17. Z. Zheng, J. Chen, Y. Wang, X. Wang, X. Chen, P. Liu, J. Xu, W. Xie, H. Chen, S. Deng, N. Xu, Highly confined and tunable hyperbolic phonon polaritons in van Der Waals semiconducting transition metal oxides. *Adv. Mater.* **30**, e1705318 (2018). doi:10.1002/adma.201705318 Medline

18. Z. Zheng, N. Xu, S. L. Oscurato, M. Tamagnone, F. Sun, Y. Jiang, Y. Ke, J. Chen, W. Huang, W. L. Wilson, A. Ambrosio, S. Deng, H. Chen, A mid-infrared biaxial hyperbolic van der Waals crystal. *Sci. Adv.* **5**, eaav8690 (2019). doi:10.1126/sciadv.aav8690 Medline

19. D. N. Basov, A. Asenjo-Garcia, P. J. Schuck, X.-Y. Zhu, A. Rubio, Polariton panorama. *Nanophotonics* **10**, 549–577 (2020). doi:10.1515/nanoph-2020-0449

20. J. D. Caldwell, I. Aharonovich, G. Cassabois, J. H. Edgar, B. Gil, D. N. Basov, Photonics with hexagonal boron nitride. *Nat. Rev. Mater.* **4**, 552–567 (2019). doi:10.1038/s41578-019-0124-1

21. A. J. Hoffman, A. Sridhar, P. X. Braun, L. Alekseyev, S. S. Howard, K. J. Franz, L. Cheng, F.-S. Choa, D. L. Sivco, V. A. Podolskiy, E. E. Narimanov, C. Gmachl, Midinfrared semiconductor optical metamaterials. *J. Appl. Phys.* **105**, 122411 (2009). doi:10.1063/1.3124087

22. G. Hu, A. Krasnok, Y. Mazor, C.-W. Qiu, A. Alù, Moiré hyperbolic metasurfaces. *Nano Lett.* **20**, 3217–3224 (2020). doi:10.1021/acs.nanolett.9b05319 Medline

23. I. Epstein, A. J. Chaves, D. A. Rhodes, B. Frank, K. Watanabe, T. Taniguchi, H. Giessen, J. C. Hone, N. M. R. Peres, F. H. L. Koppens, Highly confined in-plane propagating exciton-polaritons on monolayer semiconductors. *2D Materials* **7**, 035031 (2020). doi:10.1088/2053-1583/ab8dd4

24. P. Li, M. Lewin, A. V. Kretinin, J. D. Caldwell, K. S. Novoselov, T. Taniguchi, K. Watanabe, F. Gaussmann, T. Taubner, Hyperbolic phonon-polaritons in boron nitride for near-field optical imaging and focusing. *Nat. Commun.* **6**, 7507 (2015). doi:10.1038/ncomms8507 Medline

25. Z. Jacob, J.-Y. Kim, G. V. Naik, A. Boltasseva, E. E. Narimanov, V. M. Shalaev, Engineering photonic density of states using metamaterials. *Appl. Phys. B* **100**, 215–218 (2010). doi:10.1007/s00340-010-4096-5

26. H. N. S. Krishnamoorthy, Z. Jacob, E. Narimanov, I. Kretzschmar, V. M. Menon, Topological transitions in metamaterials. *Science* **336**, 205–209 (2012). doi:10.1126/science.1219171 Medline

27. P. Merkl, F. Mooshammer, S. Brem, A. Girnghuber, K.-Q. Lin, L. Weigl, M. Liebich, C.-K. Yong, R. Gillen, J. Maultzsch, J. M. Lupton, E. Malic, R. Huber, Twist-tailoring Coulomb correlations in van der Waals homobilayers. *Nat. Commun.* **11**, 2167 (2020). doi:10.1038/s41467-020-16069-z Medline

28. C. Poellmann, P. Steinleitner, U. Leierseder, P. Nagler, G. Plechinger, M. Porer, R. Bratschitsch, C. Schüller, T. Korn, R. Huber, Resonant internal quantum transitions and femtosecond radiative decay of excitons in monolayer WSe2. *Nat. Mater.* **14**, 889–893 (2015). doi:10.1038/nmat4356 Medline

29. T. G. Pedersen, S. Latini, K. S. Thygesen, H. Mera, B. K. Nikolić, Exciton ionization in multilayer transition-metal dichalcogenides. *New J. Phys.* **18**, 073043 (2016). doi:10.1088/1367-2630/18/7/073043

30. M. Eisele, T. L. Cocker, M. A. Huber, M. Plankl, L. Viti, D. Ercolani, L. Sorba, M. S. Vitiello, R. Huber, Ultrafast multi-terahertz nano-spectroscopy with sub-cycle temporal resolution. *Nat. Photonics* **8**, 841–845 (2014). doi:10.1038/nphoton.2014.225

31. M. Wagner, Z. Fei, A. S. McLeod, A. S. Rodin, W. Bao, E. G. Iwinski, Z. Zhao, M. Goldflam, M. Liu, G. Dominguez, M. Thiemens, M. M. Fogler, A. H. Castro Neto, C. N. Lau, S. Amarie, F. Keilmann, D. N. Basov, Ultrafast and nanoscale plasmonic phenomena in exfoliated graphene revealed by infrared pump-probe nanoscopy. *Nano Lett.* **14**, 894–900 (2014). doi:10.1021/nl4042577 Medline

32. A. S. McLeod, P. Kelly, M. D. Goldflam, Z. Gainsforth, A. J. Westphal, G. Dominguez, M. H. Thiemens, M. M. Fogler, D. N. Basov, Model for quantitative tip-enhanced spectroscopy and the extraction of nanoscale-resolved optical constants. *Phys. Rev. B* **90**, 085136 (2014). doi:10.1103/PhysRevB.90.085136

33. A. Chernikov, C. Ruppert, H. M. Hill, A. F. Rigosi, T. F. Heinz, Population inversion and giant bandgap renormalization in atomically thin WS2 layers. *Nat. Photonics* **9**, 466–470 (2015). doi:10.1038/nphoton.2015.104

34. A. J. Sternbach, S. Latini, S. Chae, H. Hübener, U. De Giovannini, Y. Shao, L. Xiong, Z. Sun, N. Shi, P. Kissin, G.-X. Ni, D. Rhodes, B. Kim, N. Yu, A. J. Millis, M. M. Fogler, P. J. Schuck, M. Lipson, X.-Y. Zhu, J. Hone, R. D. Averitt, A. Rubio, D. N. Basov, Femtosecond exciton dynamics in WSe$_2$ optical waveguides. *Nat. Commun.* **11**, 3567 (2020). doi:10.1038/s41467-020-17335-w Medline

35. J. Wang, J. Ardelean, Y. Bai, A. Steinhoff, M. Florian, F. Jahnke, X. Xu, M. Kira, J. Hone, X.-Y. Zhu, Optical generation of high carrier densities in 2D semiconductor heterobilayers. *Sci. Adv.* **5**, eaax0145 (2019). doi:10.1126/sciadv.aax0145 Medline

36. T. G. Folland, A. Fali, S. T. White, J. R. Matson, S. Liu, N. A. Aghamiri, J. H. Edgar, R. F. Haglund Jr., Y. Abate, J. D. Caldwell, Reconfigurable infrared hyperbolic metasurfaces using phase change materials. *Nat. Commun.* **9**, 4371 (2018). doi:10.1038/s41467-018-06858-y Medline

37. A. J. Sternbach, J. Hinton, T. Slusar, A. S. McLeod, M. K. Liu, A. Frenzel, M. Wagner, R. Iraheta, F. Keilmann, A. Leitenstorfer, M. Fogler, H.-T. Kim, R. D. Averitt, D. N. Basov, Artifact free time resolved near-field spectroscopy. *Opt. Express* **25**, 28589–28611 (2017). doi:10.1364/OE.25.028589

38. D. Edelberg, D. Rhodes, A. Kerelsky, B. Kim, J. Wang, A. Zangiabadi, C. Kim, A. Abhinandan, J. Ardelean, M. Scully, D. Scullion, L. Embon, R. Zu, E. J. G. Santos, L. Balicas, C. Marianetti, K. Barmak, X. Zhu, J. Hone, A. N. Pasupathy, Approaching the intrinsic limit in transition metal diselenides via point defect control. *Nano Lett.* **19**, 4371–4379 (2019). doi:10.1021/acs.nanolett.9b00985 Medline

39. F. L. Ruta, A. J. Sternbach, A. B. Dieng, A. S. McLeod, D. N. Basov, Quantitative nanoinfrared spectroscopy of anisotropic van der Waals materials. *Nano Lett.* **20**, 7933–7940 (2020). doi:10.1021/acs.nanolett.0c02671 Medline

40. S. T. Chui, X. Chen, H. Hu, D. Hu, Q. Dai, M. Liu, Photo-induced charge density distribution in metal surfaces and its extraction with apertureless near-field optics. *J. Phys. Condens. Matter* **31**, 24LT01 (2019). doi:10.1088/1361-648X/ab0fb3 Medline

41. S. Dai, Q. Ma, T. Andersen, A. S. Mcleod, Z. Fei, M. K. Liu, M. Wagner, K. Watanabe, T. Taniguchi, M. Thiemens, F. Keilmann, P. Jarillo-Herrero, M. M. Fogler, D. N. Basov, Subdiffractional focusing and guiding of polaritonic rays in a natural hyperbolic material. *Nat. Commun.* **6**, 6963 (2015). doi:10.1038/ncomms7963 Medline

42. S. Latini, T. Olsen, K. S. Thygesen, Excitons in van der Waals heterostructures: The important role of dielectric screening. *Phys. Rev. B Condens. Matter Mater. Phys.* **92**, 245123 (2015). doi:10.1103/PhysRevB.92.245123

43. K. Andersen, S. Latini, K. S. Thygesen, Dielectric genome of van der Waals heterostructures. *Nano Lett.* **15**, 4616–4621 (2015). doi:10.1021/acs.nanolett.5b01251 Medline

44. X. Andrade, D. Strubbe, U. De Giovannini, A. H. Larsen, M. J. T. Oliveira, J. Alberdi-Rodriguez, A. Varas, I. Theophilou, N. Helbig, M. J. Verstraete, L. Stella, F. Nogueira, A. Aspuru-Guzik, A. Castro, M. A. L. Marques, A. Rubio, Real-space grids and the Octopus code as tools for the development of new simulation approaches for electronic systems. *Phys. Chem. Chem. Phys.* **17**, 31371–31396 (2015). doi:10.1039/C5CP00351B Medline